GECT - Gene Expression Detection in Developing Tissue Using µCT Imaging

Vilma Väänänen[1], Mona M. Christensen[1], Heikki Suhonen[2], Jukka Jernvall[1,3]

[1]Institute of Biotechnology, University of Helsinki, P.O. Box 56, FI-00014 Helsinki, Finland

[2] Department of Physics, University of Helsinki, P.O. Box 64, FI-00014 Helsinki, Finland

[3]Department of Geosciences and Geography, University of Helsinki, P.O. Box 64, FI-00014 Helsinki, Finland

Correspondence

Institute of Biotechnology, University of Helsinki, P.O. Box 56, FI-00014 Helsinki, Finland

Email: vilma.k.vaananen@helsinki.fi

Abstract

High resolution and noninvasiveness have made soft tissue X-ray microtomography (µCT) a widely applicable three-dimensional (3D) imaging method in studies of morphology and development. However, scarcity of molecular probes to visualize gene activity with µCT has remained a challenge. Here we apply horseradish peroxidase -assisted reduction of silver and catalytic gold enhancement of the silver deposit to *in situ* hybridization in order to detect gene expression in developing tissues with µCT (here called GECT, Gene Expression CT). We show that GECT detects expression patterns of *collagen type II alpha 1 (Col2a1*) and *sonic hedgehog (Shh*) in developing mouse tissues comparably with an alkaline phosphatase-based detection method. After detection, expression patterns are visualized with laboratory µCT, demonstrating that GECT is compatible with varying levels of gene expression and varying sizes of expression regions. Additionally, we show that the method is compatible with prior phosphotungstic acid (PTA) staining, a conventional contrast staining approach in µCT imaging of soft tissues. Overall, GECT is a method that can be integrated with existing laboratory routines to obtain spatially accurate 3D detection of gene expression.

Keywords

µCT imaging, development, gene expression, *in situ* hybridization

Introduction

Studies of animal morphology and development require accurate visual information of three-dimensional structures that are typically too opaque for visible-light imaging. X-ray imaging methods are highly suitable for this purpose due to their penetrance and high, uniform resolution. One of the currently most accessible formats of 3D X-ray imaging is X-ray microtomography (µCT), which allows microscale resolution imaging of intact samples with relatively straightforward sample preparation using benchtop imaging equipment.

In X-ray attenuation µCT, X-ray projections of the sample are collected in various angles and then used to computationally generate a 3D model of how the sample reduces intensity of the X-rays traveling through it (Mizutani & Suzuki, 2012; Rawson et al., 2020). As the X-ray attenuation is considered proportional to the electron density and atomic number (Z) of the elements in imaged tissue, quantifiable volumetric data is obtained (Mizutani & Suzuki, 2012). 3D X-ray imaging techniques are readily applicable to nanoscale resolution imaging with techniques utilizing high-brightness synchrotron radiation, but nanoCT approaches without the need for synchrotron access are also currently available (Rawson et al., 2020). High-resolution X-ray imaging techniques allow phase contrast imaging, which has the practical benefit of samples not needing to go through any contrast enhancement procedures prior imaging (Mizutani & Suzuki, 2012; Rawson et al., 2020)

Due to intrinsic low X-ray attenuation of soft tissue, attenuation-based µCT using polychromatic X-ray sources often require procedures to increase contrast (Mizutani & Suzuki, 2012). This can be in some instances achieved by critical point drying (Zysk et al., 2012), but more widely utilized method is the use of high atomic number contrast agents (Mizutani & Suzuki, 2012; Pauwels et al., 2013)

Presence of the contrast agent in the tissue increases X-ray absorption of the sample in an energy-dependent manner (Mizutani & Suzuki, 2012; Rawson et al., 2020). Imaging a stained sample with X-ray energies near the k-shell electron binding energy of contrast agent atoms results in sudden increase in X-ray absorption, a phenomenon referred to as K-absorption edge (K-edge). K-edge

increases as the atomic number of the element increases, and many of the established X-ray imaging applications rely on contrast agents with high atomic number. Commonly used contrast agents include iodine (Z=53, K-edge 33.2 keV) and tungsten (phosphotungstic acid, PTA, Z=74, K-edge 69.5 keV), both recommended due to their ease of use and low toxicity (Metscher, 2009b, 2009a; Pauwels et al., 2013). More recently, eosin, a common compound used in histology, was shown to generate high contrast suitable for high-resolution X-ray imaging of mouse kidney (Busse et al., 2018). Bromine (Z=35, K-edge 13.5 keV) present in eosin molecules generates X-ray attenuation during μCT imaging (Busse et al., 2018). Applying similar idea of utilizing conventional histological stains as μCT contrast agents, a method was described based on the use of hematein in complex with led (Z =82, K-edge 88 keV) for high-resolution nanoCT imaging of mouse liver and subsequent histological sectioning (Müller et al., 2018). Yet another contrast agent is protargol, a silver-protein compound that has been used as a general tissue contrast stain in synchrotron μCT imaging of tooth development (Raj et al., 2014). Silver has atomic number of 47 and K-edge of 25.5 keV, which translates to higher X-ray absorption in silver containing regions compared to unstained tissue when imaged with X-ray energies near 25.5 keV. Compared to conventional PTA staining, protargol enabled high quality imaging of early stage embryos, but suffered the same penetration problems as does PTA when imaging was extended to older whole embryo heads and intact embryos (Raj et al., 2014).

In contrast to the imaging of tissues, a long-standing challenge in biological μCT imaging has been the limited number of methods available to detect specific molecules or gene activity. Quite recently, enhancement of metal 3,3-diaminobenzidine detection (nickel/cobalt DAB) with osmium tetroxide and uranyl acetate was used in the visualization of Ret antibody in wild type and mutant mice (Hoshi et al., 2018). Enhanced DAB detection was also the basis of a method where use of peroxidase reporter gene enabled staining of specific cell populations in Drosophila legs and mouse brain (Kuan et al., 2020). Also, a LacZ reporter gene system was recently established for μCT imaging of gene expression, utilizing the radiodensity of bromine in the product of the β-galactosidase reaction (Ermakova et al., 2021).

Silver has demonstrated potential also as a more specific contrast stain for X-ray imaging. Recently, modified Fontana-Masson staining was used for 3D detection and quantification of melanin content in zebrafish larvae (Katz et al., 2021). Immunohistochemical approach by Metscher & Müller (2011) utilized peroxidase-facilitated reduction of silver ions on sites of target proteins, and the 3D distribution of collagen type 2 and acetylated alpha tubulin in chick embryos was then visualized with µCT imaging.

Despite these advances, detection of gene expression, a central focus of developmental biology studies, remains challenging using µCT in a way that can be integrated with existing laboratory routines. To this end, here were introduce a method for the detection of gene expression in messenger RNA (mRNA) level, utilizing peroxidase-assisted reduction of silver in *in situ* hybridization.

A Gene Expression CT (GECT) method to detect gene expression in developing tissues

To explore the usefulness of silver-based methods for visualization of gene expression using attenuation µCT, we detected the expression of two genes, *collagen type 2 alpha 1* (*Col2a1*) and *sonic hedgehog (Shh)*, in embryonic tissues of mouse using silver reducing *in situ* hybridization. We then compared the resulting expression patterns to conventional chromogenic *in situ* hybridization done in parallel with silver detection (Fig 1A, B.)

In both *in situ* hybridization approaches, mRNA of interest is detected with digoxigenin (DIG)-labeled RNA-probes. Whereas in chromogenic *in situ* hybridization the detection is based on alkaline phosphatase activity, silver *in situ* hybridization utilizes anti-DIG antibody conjugated to horseradish peroxidase (HRP) (Fig 1C). HRP facilitates specific reduction of silver ions in solution on sites of gene activity. In the presence of reducer, elemental silver condensates are formed (Powell et al., 2002, 2007). (Fig 1C).

Compared to proteins distributed abundantly, the general challenge in imaging gene expression is the detection of transient and intracellular messenger RNA (mRNA). Silver has K-absorption edge

111 in the lower end of the standard µCT energy spectrum, a challenge in case the molecule of interest
112 is present in very low numbers. Therefore, to increase the X-ray absorption of the expression sites,
113 we utilized a commercial gold enhancement kit (Nanoprobes) to strengthen the expression signal
114 and compared the resulting expression patterns to the conventional chromogenic method (Fig 1D).

115 Gold enhancement is based on autometallography, where metal ions are catalytically reduced on
116 the surface of already existing metal particles in the presence of a reducer (Danscher, 1984;
117 Grizzle, 1996). Commercial gold enhancement protocols do not state exact components of the
118 detection reaction (Hainfeld et al., 1999; Weipoltshammer & Schöfer, 2000), but contain a set of
119 solutions called "enhancer", "activator" and "initiator" and buffer (Hainfeld et al., 1999;
120 Weipoltshammer & Schöfer, 2000). Sodium thiosulphate washes reduce the background staining
121 and stop the detection reaction (Hainfeld et al., 1999). We aimed to enhance the silver precipitate
122 generated by peroxidase assisted silver reduction with elemental gold (Z=79, K-edge 80.7 keV),
123 and thus increase the electron density of the expression sites towards a range suitable for routine
124 µCT visualization.

125 To test whether our approach can detect widespread expression fairly deep inside tissue, we
126 conducted *in situ* hybridization for *collagen type 2 alpha 1* (*Col2a1*) for whole embryonic day 12.5
127 mouse embryo (Fig 1). This should provide largely comparable patterns to the type II collagen
128 protein detected in embryonic chicken previously using µCT (Metscher & Müller, 2011). During
129 later embryogenesis after embryonic day 12*, Col2a1* is a prominent marker of differentiating
130 chondrocytes in the developing skeletal system (Cheah et al., 1991; Ng et al., 1997; Sandberg &
131 Vuorio, 1987). More specifically, *Col2a1* is highly expressed in developing digits and limbs,
132 developing vertebrae and ribs and developing parietal and occipital bones of skull (Sakai et al.,
133 2001).

134 To challenge the method in conditions where the target molecule is expressed locally and in low
135 numbers, we show that GECT can be used to visualize expression of *sonic hedgehog* (*Shh*) in a
136 developing tooth germ of embryonic mouse (Fig 1). *Shh* is a central gene in the development of
137 several mammalian organ systems, including ectodermal appendages such as teeth, hair buds and

138 taste buds (Bitgood & McMahon, 1995; Dassule et al., 2000; Hallikas et al., 2021). During mouse
139 embryonic day 14 to 15, *Shh* is expressed in the embryonic signaling center of a tooth germ, called
140 the primary enamel knot (Jernvall et al., 1998; Jernvall et al., 1994).

141 To further establish the method as a way to visualize 3D gene expression and tissue morphology
142 from an individual tissue sample, we combine phosphotungstic acid staining and µCT imaging of
143 3D morphology to the detection pipeline, from now on called GECT (Gene Expression CT) (Fig
144 1E).

145

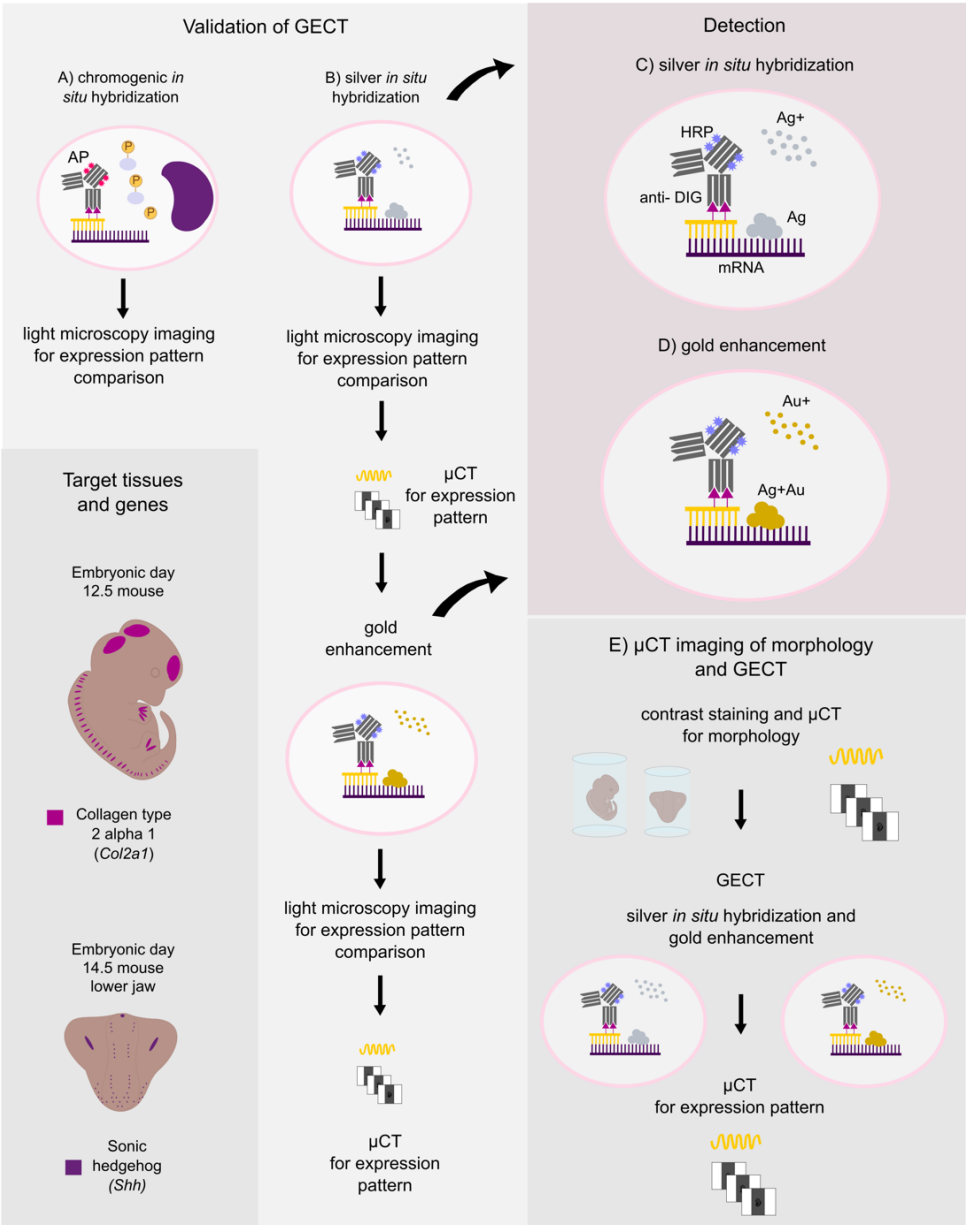

146

147 **Figure 1. Validation of Gene Expression CT (GECT) and the pipeline for µCT imaging of morphology**
148 **and gene expression.** Validation was conducted by performing chromogenic (A) and silver (B) *in situ*
149 hybridizations in parallel followed by the gold enhancement on the silver *in situ* samples. C) Silver detection
150 was conducted with horseradish peroxidase (HRP) conjugated anti- DIG antibody and standard commercial
151 detection kit (EnzMet, enzymatic metallography, Nanoprobes). During detection, HRP facilitates reduction of
152 silver ions on sites of antibody (and probe) binding. D) Gold enhancement (Gold Enhancement for LM,
153 Nanoprobes) utilizes the silver condensates in the tissue as seeding particles and covers them with
154 elemental gold by reducing gold ions in solution. Resulting signal was imaged with light microscopy and µCT.
155 Some samples underwent µCT after silver *in situ* hybridization (C) and all samples underwent µCT after gold
156 enhancement (D). E) To further validate the detection scheme for routine use, we stained additional samples
157 with phosphotungstic acid, imaged them with µCT to obtain representation of 3D morphology and conducted
158 gene expression detection after µCT imaging for morphology.

Methods

Ethics statement

All animal work was performed in accordance with the guidelines of the Finnish Authorization Board under licenses KEK16-021 and KEK19-019.

Animal work

Wild type NMRI mice (Envigo) were used for collection of tissue samples. Embryonic age was determined as days from the appearance of the vaginal plug (day 0). Embryos were fixed overnight using 4 % paraformaldehyde in 1x phosphate buffered saline (PBS), + 4 °C. Lower jaws were dissected in Dulbecco's phosphate buffered saline under light microscope before overnight fixation with 4 % PFA in +4 °C. Samples were dehydrated via methanol series and stored in 100 % methanol - 20°C.

Phosphotungstic acid staining

Samples were rehydrated from 100 % MeOH to 70 % EtOH and stained with 0.3 % phosphotungstic acid (PTA) in 70 % EtOH for 24 - 48 hours in + 8 °C (Metscher, 2009a). After staining, samples were returned to 70 % EtOH. X-ray imaging of PTA -stained samples was conducted in 70 % EtOH using 1.6 mL polypropylene tubes with screw cap and seal (Cryopure, Sarstedt). Samples were stored 70 % EtOH in +4 °C until proceeding with *in situ* hybridization.

Probe preparation and in vitro transcription

Digoxigenin - conjugated RNA probes specific for mouse (*Mus musculus*) *collagen type 2 alpha 1* (*Col2a1*) were generated according to Metsäranta et al., 1991. Plasmid construct (Bluescript KS-, Strategene) for mouse *Col2a1* mRNA probes (405 bp) was provided by Mikkola lab, Institute of Biotechnology.

Digoxigenin - conjugated RNA probes specific to mouse (*Mus musculus*) *sonic hedgehog* – gene (*Shh*) exons 1, 2 and 3 were generated using the following primers: CGTAAGTCCTTCACCAGCTTG (forward) and GCTGACCCCTTTAGCCTACA (reverse). Plasmid

184 construct (Topo PCR II, Invitrogen) for mouse *Shh* mRNA probes (543 bp) was provided by
185 Jernvall lab, Institute of Biotechnology. Specificity of target mRNA binding was confirmed using a
186 sense probe in slide *in situ* hybridization and in whole mount *in situ* hybridization, both
187 chromogenic and metallographic detection were used.

188 *Whole mount in situ hybridization*

189 Steps were conducted in 24-well plate (Cellstar, Greiner Bio-One) in a volume of 900 µL unless
190 otherwise stated. Samples stored in 100 % methanol were rehydrated to 1x PBS with 0.1%
191 Tween20 (Sigma- Aldrich, P7949-500ML) through a descending methanol series. Ethanol series
192 was used for samples that had been stained with phosphotungstic acid and imaged with µCT prior
193 *in situ* hybridization. After three 15 -minute washes in 1x PBS-T, samples were incubated in 3 %
194 hydrogen peroxide (Honeywell, ref in 1x PBS-T for 1 h in room temperature (RT). Samples were
195 washed four times with 1x PBS-T for 15 minutes, and then incubated with 10 µg / mL of Proteinase
196 K (Roche, ref 03115879001) in 1x PBS-T, followed by two 10-minute washes with 2 mg / mL
197 glycine (Sigma Life Science, G8790-100G) in 1x PBS-T. After four 15-minute washes with 1x PBS-
198 T, samples were incubated in 4 % PFA in 1x PBS for 20 minutes, followed by three 15-minute
199 washes with 1x PBS-T.

200 Hybridization step and incubation with antibody were conducted in 2 mL tubes to allow the solution
201 to mix evenly during the incubation period. Hybridization was carried out overnight at + 65 °C with
202 rocking, using probes for mouse *sonic hedgehog* (*Shh*) and *collagen type 2 alpha 1* (*Col2a1*)
203 (Metsäranta et al., 1991) with a concentration of 1 µg / mL. After hybridization, samples were
204 washed two times in 50 % formamide (Emsure, ref 1.09684.1000, Merck), 5x saline sodium citrate
205 (SSC) buffer, 1 % SDS - solution for 30 minutes and 3 times in 50 % formamide, 2x SSC- solution
206 for 30 minutes. All washes were conducted in + 65 °C.

207 Before antibody incubation, samples were washed in 1x maleic acid buffer (MABT). Anti-DIG
208 antibody conjugated with HRP (Roche) was diluted 1 in 50 in solution consisting of 2 % blocking
209 reagent (Roche ref 11096176001), 1 % goat serum (Gibco, ref 16210-064) in 1x MABT. Alkaline

210 phosphatase (AP) conjugated anti-DIG antibody (Roche, ref 11207733910) was diluted 1 in 2000.
211 After addition of the antibody, samples were incubated overnight in + 4 °C with rocking and then
212 washed with 1x MABT for three times 15 minutes, three times 20 minutes, three times 40 minutes
213 and for one hour, RT.

214 To detect *Shh* and *Col2a1* using alkaline phosphatase activity, BM Purple AP substrate (Roche, ref
215 11096176001) was added to the samples with AP-conjugated DIG-antibody. Samples were first
216 washed with AP buffer (100mM Tris pH 9.5, 100mM NaCl, 50mM $MgCl_2$, 0.1 % Tween20 for 10
217 minutes and 20 minutes RT before adding the substrate. After substrate addition, samples were
218 incubated in room temperature and protected from light until strong signal was detected (1-4 hours
219 with *Col2a1* mouse embryos, 15-18 hours with *Shh* in mouse embryonic lower jaws). After washing
220 the samples with 1x PBS for 3 x 10 minutes, samples were fixed with 4 % PFA in 1x PBS
221 overnight. Next day samples were transferred to 1x PBS for bright field imaging.

222 Horseradish peroxidase-based detection was carried out using EnzMet General HRP Detection Kit
223 (Nanoprobes, ref 6010-15mL). Before detection, samples were transferred from 1x MABT to 1:1
224 solution of 1x MABT and 100 mM sodium citrate buffer, pH 7 for five minutes, and then washed
225 with sodium citrate buffer for 3 x 15 minutes.

226 Equal volumes of solutions A, B and C of the EnzMet General HRP Detection Kit were added
227 respectively on each sample with anti-DIG antibody conjugated with HRP. 15-minute incubation
228 was conducted in between each addition of detection solution. After addition of solution C,
229 detection was monitored under light microscope until first signs of silver precipitate in solution
230 started to emerge (5-10 minutes). After HRP-based detection, samples were transferred to 1 %
231 sodium thiosulphate (Sigma-Aldrich ref 217247-25G) in deionized water and stored overnight in +
232 4 °C before bright field imaging and gold enhancement. In cases where samples were imaged with
233 µCT before proceeding with gold enhancement (Supplementary Figure 2A), samples were
234 gradually dehydrated to 70 % EtOH after bright field imaging.

235

236 *Gold enhancement*

237 Depending on whether the sample was imaged with µCT before gold enhancement, samples were
238 either directly transferred from 1 % sodium thiosulphate to 1x PBS (not µCT imaged, Figures 2-4)
239 or gradually rehydrated from 70 % EtOH to 1x PBS (µCT imaged, Supplementary Figure 2A).
240 Samples were first washed with 1x PBS for 15 minutes and then transferred to 50 mM glycine in 1x
241 PBS for 15 minutes, RT. Before reaction initiation, samples were rinsed in deionized water with
242 0.1 % Tween20 for 15 minutes, RT. Equal amounts of solutions A (Enhancer) and B (Activator) of
243 the kit (GoldEnhance for LM, ref 2112-28ML, Nanoprobes) were mixed and left to incubate
244 according to protocol provided by the manufacturer, before addition of solutions C (Initiator), D
245 (Buffer) and 0.1 % Tween20. Reagent mixture with Tween20 was added on samples and reaction
246 was developed under microscope until signal was as strong as possible without any precipitate in
247 the solution, varying from 2.5 minutes to 6 minutes. After detection, samples were rinsed in
248 deionized water with 0.1 % Tween20 for five minutes until fixing with 1 % sodium thiosulphate in
249 deionized water with a minimum of 15 minutes to overnight, RT. To test whether gold
250 enhancement could provide additional means to modulate the signal strength in µCT, the
251 procedure was repeated on lower jaw samples after µCT imaging of first gold enhancement signal.

252 *Vibratome sectioning*

253 To verify that detection components are capable of penetrating to the region of primary enamel
254 knot, jaw specimen undergone silver deposition and gold enhancement was casted in 6 % low
255 melting point agarose (TopVision, ref R0801, Thermo Scientific) in 1xPBS and sectioned to 100
256 µm sections with vibratome (Microm). Sections were collected in 6-well plate in 1x PBS and
257 imaged over glass slides mounted in aqueous mounting medium (Shandon Immumount, ref
258 9990402, Thermo Scientific). Vibratome sections were imaged using Zeiss Imager.M2 AX10 with
259 AxioCam HRc camera, EC Plan NEOFLUAR 10x objective and Zeiss Zen2 Pro blue edition
260 software. Images were oriented, cropped, and brightness and contrast were adjusted using ImageJ
261 software (Fiji) (Schindelin et al., 2012).

262 *Light microscopy imaging*

263 Bright field images of whole mount samples were taken using Zeiss Lumar V12 stereomicroscope,
264 AxiocamICc1 camera, Zeiss Zen 2012 blue edition software and Apolumar S 1.2 x objective with
265 magnification of 25 x and 12 x. Samples were transferred to 1x PBS and set on 4 % low melting
266 point agarose plate to position them. To obtain in focus images of whole sample, multidimensional
267 acquisition (Z-stack) was used with individually optimized focus plane distance and number of
268 focus planes. Extended depth of focus was achieved using highest alignment of "wavelets"-
269 function in Zeiss Zen 2012 blue edition. Images were cropped, and brightness and contrast were
270 adjusted using ImageJ software (Fiji). After bright field imaging, samples were gradually
271 dehydrated to 70 % EtOH for µCT imaging.

272 *µCT imaging*

273 X-ray imaging was conducted in 70 % EtOH using Bruker Skyscan 1272 µCT device in X-ray
274 laboratory in Department of Physics, University of Helsinki. For tomographic imaging of the overall
275 morphology of whole mouse embryos with a voxel size of 3 µm, we used 0.5 mm aluminum filter,
276 source voltage/current of 70 kV / 142 µA, rotation step of 0.1 degrees and frame averaging of 4.
277 Scanning resulted in 1922 projections over 180° with exposure time of 3038 ms. Total imaging
278 time was approximately nine hours. Samples were stored in 70 % EtOH in + 4 °C until *in situ*
279 hybridization.

280 µCT imaging after *in situ* hybridization was conducted for lower jaws in 70 % EtOH using the
281 following settings: 1 µm voxel size, no filter, source voltage/current of 30 kV / 212 µA, rotation step
282 0.1 degrees, frame averaging 5. Scanning resulted in 1877 projections over 180° with exposure
283 time of 1410 ms. Total imaging time was approximately 4.5 hours. For gold enhancement of
284 embryonic lower jaws, a voxel size of 3 µm was used with 0.25 aluminum filter, source
285 voltage/current of 60 kV / 166 µA, rotation step of 0.1 degrees and frame averaging of 5. Scanning
286 resulted in 1922 projections over 180° with exposure time of 1060 ms. Total imaging time was
287 approximately four hours. For µCT imaging of gold enhanced embryos, we used a 3 µm voxel size,

288 0.25 mm aluminum filter, source voltage/current of 60 kV /166 µA, rotation step of 0.1 degrees and
289 frame averaging of 4. Scanning resulted in 1992 projections over 180° with exposure time of 2269
290 ms. Total imaging time was approximately seven hours.

291 *Reconstruction and post-processing*

292 Reconstruction of the µCT data was conducted with nRecon – software (1.7.4.2) with misalignment
293 compensation and ring artifact correction optimized separately for each dataset. Regions of
294 interest were reconstructed as 16- bit tiff stacks that were reoriented and cropped in ImageJ (Fiji)
295 before volume rendering and segmentation in Avizo.

296 *Segmentation*

297 Segmentation of expression regions was conducted in Avizo (rel 9.0.1) by first excluding 20 % of
298 the darkest pixels in the reconstruction (jaw) and 25 % of the darkest pixels in the reconstruction
299 (whole embryo) by using Thresholding- tool available in Avizo Segmentation- view and then by
300 manually excluding pixels with Brush- tool in Segmentation – view. Pixels were excluded from
301 expression regions based on evaluation where light microscopy data from chromogenic *in situ*
302 hybridization, silver in *situ* hybridization and gold enhancement was considered together with the
303 location of the signal. In other words, high-intensity pixels on the surface of the specimen and in
304 inconsistent locations throughout detections were considered background and therefore excluded.
305 Extracted volume of expression region was derived by assigning a value of 1 for the segmented
306 voxels and a value of 0 for the voxels remaining outside signal region in the reconstruction volume
307 using the Arithmetic–tool in Avizo. Volume rendering and segmentation images were generated
308 with Avizo using Snapshot- tool as 16-bit tiffs. Images were cropped and oriented and brightness
309 and contrast were adjusted in ImageJ (Fiji).

310

311 **Results**

312 For the detection of an abundantly expressed gene, we tested silver *in situ* hybridization and gold
313 enhancement for *Col2a1* in embryonic day 12.5 mouse. Chromogenic detection of *Col2a1* (Fig 2A,
314 n=2) is consistent with silver detection and gold enhancement (Fig 2B-C, n=2), showing expression
315 in developing cartilage of limbs, spine and skull. Combination of gold and silver in detection of
316 *Col2a1* enables visualization of expression via µCT (Fig 2D). Expression of *Col2a1* is particularly
317 clear in limbs of the developing embryo, as shown in the upper limb in Figures 2E-H. The silver *in*
318 *situ* hybridization and gold enhancement generate a clear-cut signal, from which interphalangeal
319 joint spaces are distinguishable as non-expressing tissue (Fig 2F-H).

320 To test visualization of both the tissue morphology and the gene expression in the same sample,
321 we applied silver *in situ* hybridization and gold enhancement to samples that had undergone
322 phosphotungstic acid (PTA) staining and µCT imaging for morphology. Compared to control
323 samples without PTA staining prior to *in situ* hybridization (Fig 3A-B, n=2), PTA-stained samples
324 replicated the expected expression pattern of *Col2a1* in both stages of detection (Fig 3C-D),
325 similarly with slight increase in background when gold enhancement was applied. µCT
326 reconstruction of the PTA-stained sample prior *in situ* hybridization shows good contrast between
327 the sample and the scanning medium (Fig 3E) and between tissue compartments (Fig 3F). Gold
328 enhanced signal of *Col2a1* expression from the same sample was detectable with µCT (Fig 3G)
329 and segmented expression regions inside the hindlimb are shown in Figure 3H and 3I and
330 Supplementary video 1.

331

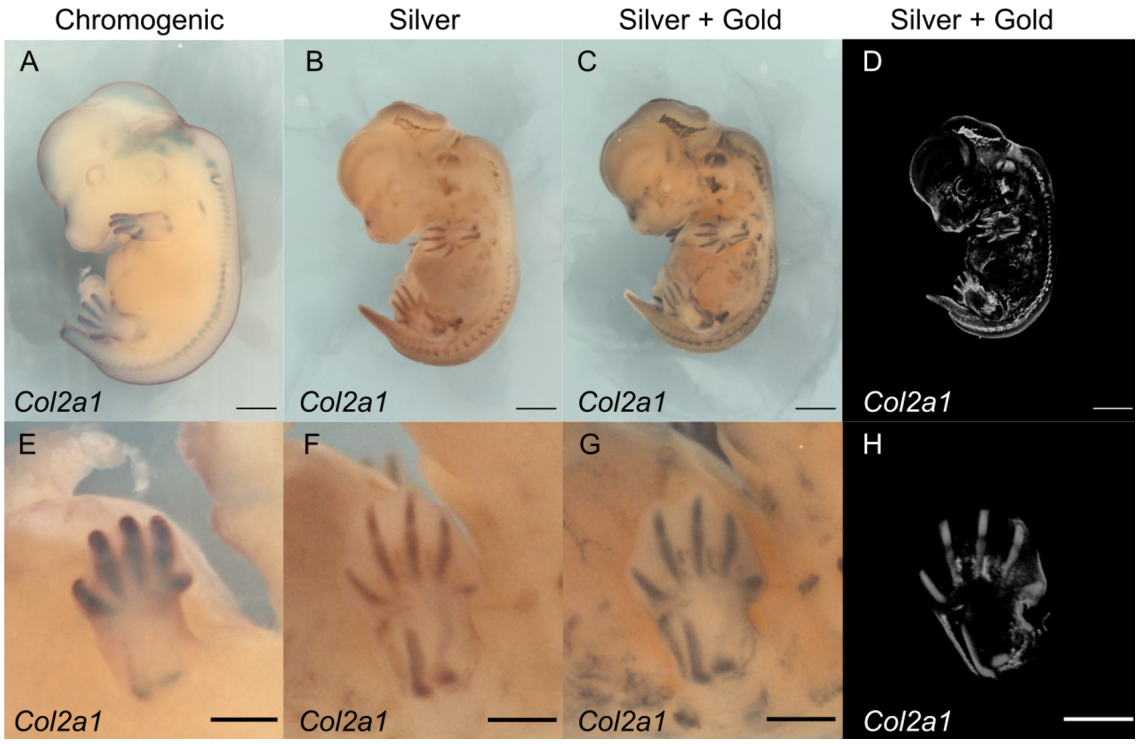

332

333 **Figure 2. Detection of *Collagen type 2 alpha 1 (Col2a1*) expression with µCT.** A) Chromogenic *in situ*
334 hybridization of *Col2a1* in e12.5 mouse embryo. B) Silver *in situ* hybridization of *Col2a1*. C) Gold
335 enhancement of silver *in situ* hybridization shown in B. D) Volume rendering of *Col2a1* expression shown in
336 C. E) Close-up of left upper limb shown in A. F) Close-up of left upper limb shown in B. G) Close-up of left
337 upper limb shown in C. H) Close-up of left upper limb shown in H. Scale 1000 µm in A-D, 500 µm in E-H.

338

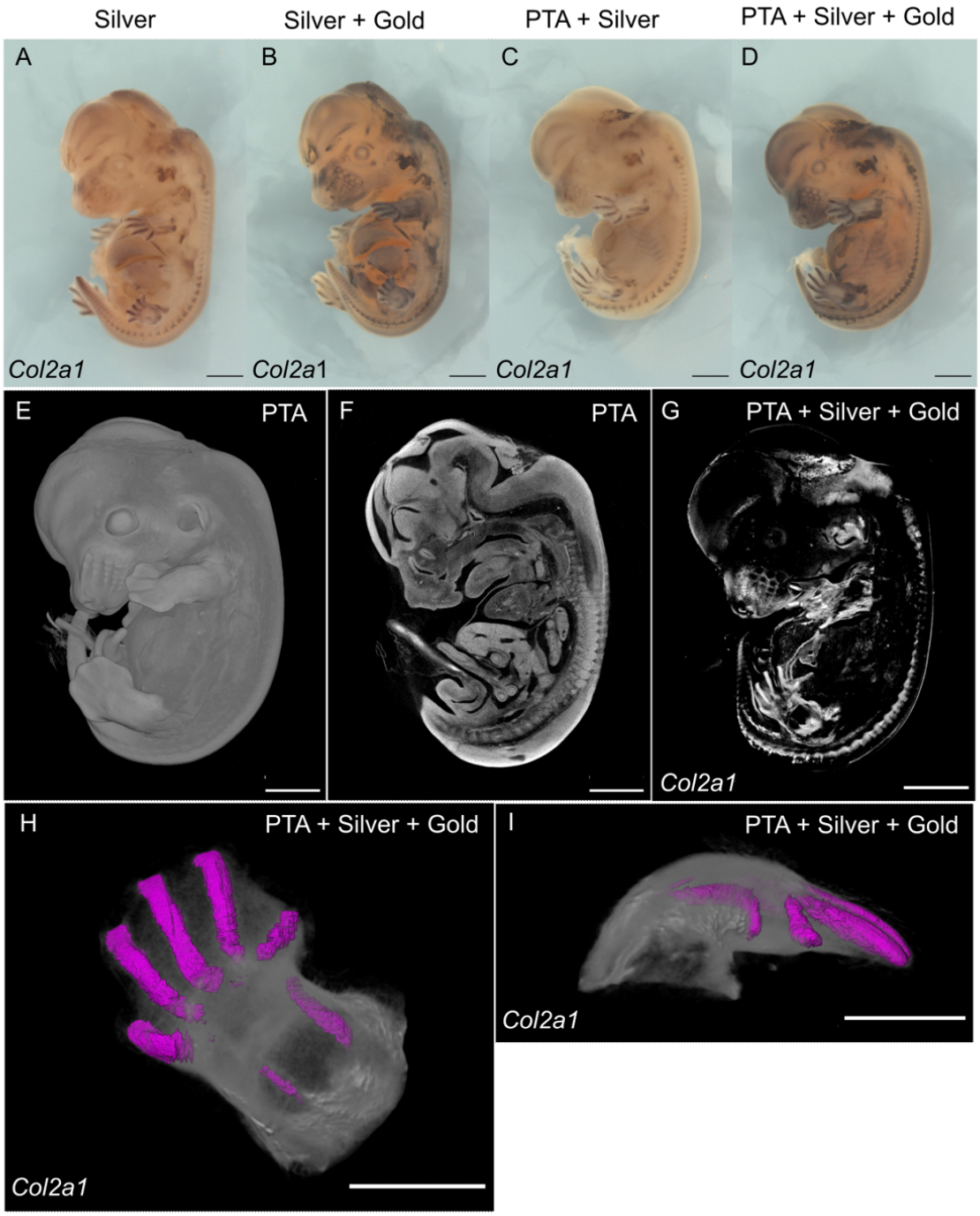

Figure 3. Tissue contrast staining before gene expression detection. A) Silver *in situ* hybridization of *Col2a1* without prior PTA stain. B) Gold enhancement of *Col2a1* detection shown in A. C) Silver *in situ* hybridization of *Col2a1* in mouse embryo stained with PTA. D) Gold enhancement of *Col2a1* detection shown in C. E) Volume rendering of the contrast-stained mouse embryo, prior *in situ* hybridization. F) Cross-section of the mouse embryo shown in E. G) Volume rendering of *Col2a1* expression shown in D. H) Close-up of left hindlimb shown in G. Segmented *Col2a1* expression inside the limb shown in magenta, sagittal view. I) Segmented *Col2a1* expression (magenta) inside left hindlimb, transverse view. Scale 1000 µm in A-G, 500 µm in H-I.

348 To focus on locally and transiently expressed developmental genes, we examined *Shh* expression
349 in developing mouse lower jaws. In the embryonic day 14 lower jaw samples including tongue*, Shh*
350 expression is detected with chromogenic *in situ* hybridization in enamel knots of the molars, hair
351 and whisker buds of the chin and taste papillae of the tongue. (Fig 4A, n=2). Silver *in situ*
352 hybridization replicates this pattern (Fig 4B, n=3) and gold enhancement of the silver detection
353 preserves it (Fig 4C, n=3). Silver *in situ* hybridization performed equally to chromogenic detection
354 in every trial (see Supplementary Table 1). We also observed that *Shh* expression regions
355 detected with silver *in situ* hybridization and gold enhancement are more spatially defined
356 compared to the signal produced by chromogenic detection (Fig 4A-C, see also Supplementary
357 Figure 1).

358 µCT imaging of jaw samples was conducted after both silver *in situ* hybridization and gold
359 enhancement. µCT imaging of silver detection resulted in no observable attenuation on sites of
360 *Shh* expression and imaging after first gold enhancement round visualized expression regions only
361 partially. (Supplementary Figure 2). In samples containing tongue, all expression sites were visible
362 with µCT after repeating gold enhancement (Fig 4D-F, *Shh* in enamel knot shown in teal color).

363 Similarly to the *Col2a1*, *Shh* expression was detectable in the tissues stained with PTA (Fig 4G-H,
364 n=2) and visible in µCT (4I, n=2). We note that whereas PTA staining before *in situ* hybridization
365 provided contrast for µCT detection of jaw tissue (Fig 4J, 4K), PTA is washed away from tissues
366 during *in situ* hybridization (Fig 4I).

367 *In situ* hybridization treatments cause tissue distortion, which may affect 3D reconstructions. When
368 compared to frontal virtual section of developing molar from jaw stained with PTA and imaged with
369 µCT (Fig 4K), frontal vibratome section of a whole mount sample undergone *in situ* hybridization
370 and gold enhancement shows tearing of surface epithelium on site of dental chord (arrow, Fig 4L).
371 Expression region of *Shh* in whole mount samples is consistent with section *in situ* hybridization
372 (Supplementary Fig 1). Epithelial tearing occurred frequently in jaw samples and also in samples
373 undergone chromogenic detection, and is thus not specific to the steps of gold enhancement. We
374 observed no drastic tearing or distortion of tissues in whole embryo samples on sites of

375 expression. Control sample without prior PTA staining shown in Fig 3A and B exhibits the extent of
376 tearing in stomach region that occurred during *Col2a1* detection. Samples stained with PTA prior
377 detection show slightly less tissue tearing (Fig 3C -D).

378

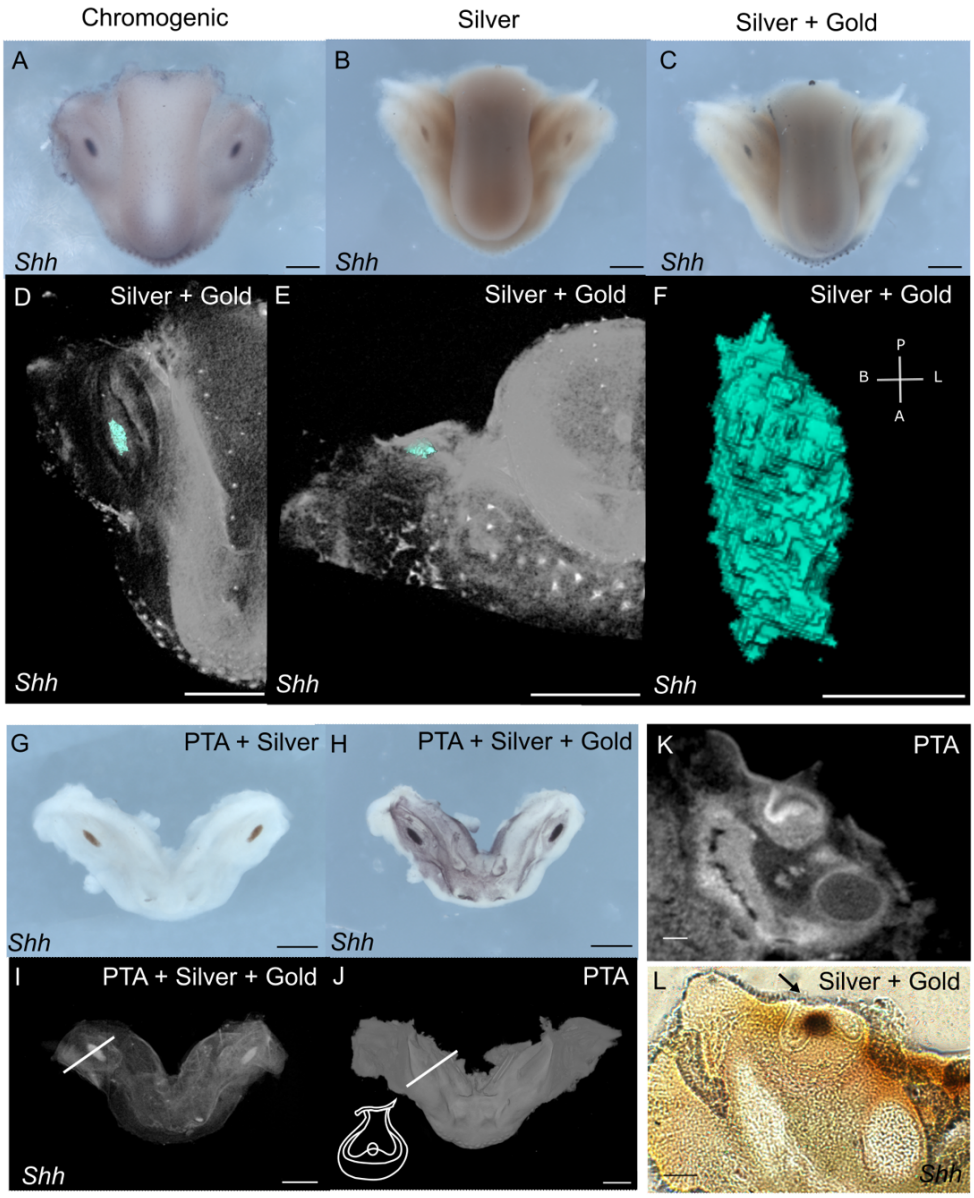

Fig 4. µCT visualization of *Sonic hedgehog (Shh)* expression from unstained and contrast-stained tissues. A) Chromogenic *in situ* hybridization of *Shh* expression in mouse e14.5 jaw. B) Silver *in situ* hybridization of *Shh*. C) Gold enhancement of *Shh* detection shown in B. D) Volume rendering of *Shh* expression from µCT data, occlusal view. Expression in embryonic molar shown in teal. E) Volume rendering of *Shh* expression, expression in embryonic molar shown in teal. frontal view. F) Segmented expression region of *Shh* in mouse molar, occlusal view. B = buccal, L = lingual A = anterior, P = posterior. G) Silver *in situ* hybridization for *Shh* applied to contrast-stained jaw. H) Gold enhancement of *Shh* detection shown in G. I) Volume rendering of µCT data from jaw shown in H. J) Volume rendering of contrast stained jaw shown in G, H and I, prior Shh detection. White line shows approximate section plane shown in K. Structures of a developing molar in shown plane are visualized in schematic in the lower left corner. K) Frontal virtual section of developing molar stained with PTA. EK = enamel knot. L) Frontal vibratome section of jaw undergone silver *in situ* hybridization and gold enhancement for *Shh* (dark brown). EK = enamel knot. Epithelial tearing shown with arrow. Scale 500 µm in A-E, 100 µm in F, 500 µm in G-J, 100 µm in K-L.

393 ## Discussion

394 Despite the wide range of resolution available in µCT imaging, there remains the challenge to
395 image specific molecules or gene activity. Initially peroxidase-assisted reduction of silver was used
396 to visualize distribution of collagen type II and acetylated alpha-tubulin proteins in chick embryos
397 with silver (Metscher & Müller, 2011). This approach utilized conventional immunohistochemical
398 detection of proteins, in which antibody is conjugated with horseradish peroxidase (Powell et al.,
399 2007). Here we apply a similar, straightforward approach to detection and visualization of mRNA
400 distribution in whole mount samples.

401 In addition to the lack of molecular markers, contrast agent use and development for µCT imaging
402 is still regarded to be in its early stages compared to other imaging modalities (Rawson et al.,
403 2020). Here our aim was to develop a method that can be incorporated into existing pipelines of i)
404 µCT imaging of soft tissue ii) detection of gene expression with *in situ* hybridization. We show that
405 the commonly used phosphotungstic acid staining can be performed prior to GECT. With two
406 rounds of µCT imaging it will be possible to obtain first the tissue structure and then, after the *in*
407 *situ* hybridization, gene expression pattern in 3D.

408 *In situ* hybridization is a robust, widely used method for spatial detection of gene expression and
409 there exists a variety of optimized protocols for a range of model organisms and both for tissue
410 sections and whole mount samples (Acloque et al., 2008; Hafen et al., 1983; Hemmati-Brivanlou et
411 al., 1990; Rosen & Beddington, 1993; Schulte-Merker et al., 1992; Thisse & Thisse, 2008; Yu &
412 Holland, 2009). The pipeline presented here requires relatively small changes to the existing *in situ*
413 hybridization pipelines. Compared to the commonly used chromogenic detection of gene
414 expression patterns, silver *in situ* hybridization provides more precise spatial readout of gene
415 expression (Fig 2 and 4, Supplementary Figure 1, (Powell et al., 2007). An added advantage is that
416 if µCT imaging is not required, the pipeline can be stopped after the silver detection and the
417 samples can be sectioned for histological analyses.

418 Areas benefitting from further developments include tissue distortion caused by *in situ*
419 hybridization. Whereas in developing mouse molars there is tearing of epithelium after *in situ*
420 hybridization, whole mouse embryos hold their shape better, exhibiting only a slight tearing in the
421 stomach. It is conceivable that these are not caused by any distinct step in the protocol but stem
422 from repeated processing of the samples. One easily modifiable aspect would be the length and
423 number of dehydration and rehydration steps preceding µCT and *in situ* hybridization. Time
424 required for sample collection, tissue staining, µCT imaging of morphology, *in situ* hybridization
425 and µCT imaging of gene expression presented in this proof-of-concept work is approximately two
426 weeks and it has room for further developments. Based on different responses of the samples we
427 used, we additionally suggest that distortion is somewhat dependent on sample size and type.
428 Specific knowledge of the target tissue allows further optimization of the detection conditions.

429 Additional potential benefit of lengthening the steps of the protocol is better penetration of detection
430 molecules, especially with large samples. We observed that both enzyme-assisted reduction of
431 silver and gold enhancement are fast detection reactions, and their accuracy benefits from low
432 development temperatures (room temperature or lower). We observed modest superficial
433 background signal in the samples with silver detection, consistent with the observations of
434 Metscher & Müller (2011). This background became stronger alongside the expression signal
435 when the same samples were processed through gold enhancement (Fig 2, Fig 3, Fig 4). The
436 benefit of µCT imaging in this context is also that the signal visible on the surface of the sample
437 can be discriminated from the signal within the sample. Nevertheless, we recommend that at least
438 when working with unfamiliar probes and genes known to have superficial expression, one should
439 run chromogenic detection alongside the combination of silver and gold detection to be able to
440 distinguish the background from the signal.

441 Metscher and Müller propose a quantification method for the level of gene expression based on the
442 intensity values of µCT imaging data (Metscher & Müller, 2011). We note that silver *in situ*
443 hybridization is an enzyme-based detection method and inherently includes variation in the
444 intensity of the signal not necessarily reflecting the biological state of the tissue. Gold

445 enhancement is not based on enzymatic activity and seems to replicate the signal of silver
446 detection faithfully, and it remains to be explored how well the method captures differences in gene
447 expression levels.

448 In conclusion, the protocol developed in this study should help to integrate μCT imaging and
449 detection of gene expression using *in situ* hybridization, two commonly used methods that when
450 combined, should provide new opportunities for biological imaging.

451 Acknowledgements

452 We thank J. Ollonen and members of the Center of Excellence in Experimental and Computational
453 Developmental Biology for advice and discussions. We thank O. Hallikas, T. Rajala, K. Väänänen
454 and L. Milocco for commenting the manuscript. We thank A. Viherä, Merja Mäkinen and Raija
455 Savolainen for technical assistance.

456 Funding

457 Financial support for this study was provided by the Academy of Finland and Doctoral Programme
458 of Integrative Life Sciences in University of Helsinki.

459 Conflicts of interest

460 The authors declare no conflicts of interest.

461 References

462 Acloque, H., Wilkinson, D. G., & Nieto, M. A. B. T.-M. in C. B. (2008). Chapter 9 In Situ
463 Hybridization Analysis of Chick Embryos in Whole- Mount and Tissue Sections. In *Avian*
464 *Embryology, 2nd Edition* (Vol. 87, pp. 169–185). Academic Press.
465 https://doi.org/https://doi.org/10.1016/S0091-679X(08)00209-4

466 Bitgood, M. J., & McMahon, A. P. (1995). Hedgehog and Bmp genes are coexpressed at many
467 diverse sites of cell-cell interaction in the mouse embryo. *Developmental Biology*, *172*(1), 126–138.
468 https://doi.org/10.1006/dbio.1995.0010

469 Busse, M., Müller, M., Kimm, M. A., Ferstl, S., Allner, S., Achterhold, K., Herzen, J., & Pfeiffer, F.
470 (2018). Three-dimensional virtual histology enabled through cytoplasm-specific X-ray stain for
471 microscopic and nanoscopic computed tomography. *Proceedings of the National Academy of*
472 *Sciences*, *115*(10), 2293–2298. https://doi.org/10.1073/pnas.1720862115

473 Cheah, K. S., Lau, E. T., Au, P. K., & Tam, P. P. (1991). Expression of the mouse alpha 1(II)
474 collagen gene is not restricted to cartilage during development. *Development*, *111*(4), 945–953.
475 https://doi.org/10.1242/dev.111.4.945

476 Danscher, G. (1984). Autometallography. *Histochemistry*, *81*(4), 331–335.
477 https://doi.org/10.1007/BF00514327

478 Dassule, H. R. H. R., Lewis, P., Bei, M., Maas, R., & McMahon, A. P. (2000). Sonic hedgehog
479 regulates growth and morphogenesis of the tooth. *Development*, *127*(22), 4775– 468 4785.
480 http://dev.biologists.org/content/127/22/4775.abstract

481 Ermakova, O., Orsini, T., Fruscoloni, P., Chiani, F., Gambadoro, A., Putti, S., Cirilli, M., Mezzi, A.,
482 Kaciulis, S., Pasquini, M., Raspa, M., Scavizzi, F., & Tocchini-Valentini, G. P. (2021). Three-
483 Dimensional X-ray Imaging of β-Galactosidase Reporter Activity by Micro-CT: Implication for
484 Quantitative Analysis of Gene Expression. *Brain Sciences*, *11*(6).
485 https://doi.org/10.3390/brainsci11060746

486 Grizzle, W. (1996). Theory and Practice of Silver Staining in Histopathology. *Journal of*
487 *Histotechnology*, *19*(3), 183–195. https://doi.org/doi: 10.1179/014788896794730568

488 Hafen, E., Levine, M., Garber, R. L., & Gehring, W. J. (1983). An improved in situ hybridization
489 method for the detection of cellular RNAs in Drosophila tissue sections and its application for
490 localizing transcripts of the homeotic Antennapedia gene complex. *The EMBO Journal*, *2*(4), 617–
491 623. https://doi.org/10.1002/j.1460-2075.1983.tb01472.x

492 Hainfeld, J. F., Powell, R. D., Stein, J. K., Hacker, G. W., Hauser-Kronberger, C., & Cheung, Annie
493 L. M. Schöfer, C. (1999). Gold-Based Autometallography. In G. W. Bailey, W. G. Jerome, S.

494 McKernan, J. F. Mansfield, & R. L. Price (Eds.), *Proceedings of the fifty-seventh Annual Meeting*,
495 *Microscopy Society of America* (pp. 486–487). Springer-Verlag.

496 Hallikas, O., Das Roy, R., Christensen, M. M., Renvoisé, E., Sulic, A.-M., & Jernvall, J. (2021).
497 System-level analyses of keystone genes required for mammalian tooth development. *Journal of*
498 *Experimental Zoology Part B: Molecular and Developmental Evolution*, *336*(1), 7–17.
499 https://doi.org/https://doi.org/10.1002/jez.b.23009

500 Hemmati-Brivanlou, A, Frank, D., Bolce, M. E., Brown, B. D., Sive, H. L., & Harland, R. M. (1990).
501 Localization of specific mRNAs in Xenopus embryos by whole-mount in situ hybridization.
502 *Development 110*(2),325 – 330. http://dev.biologists.org/content/110/2/325.abstract

503 Hoshi, M., Reginensi, A., Joens, M. S., Fitzpatrick, J. A. J., McNeill, H., & Jain, S. (2018).
504 Reciprocal Spatiotemporally Controlled Apoptosis Regulates Wolffian Duct Cloaca Fusion. *Journal*
505 *of the American Society of Nephrology*, *29*(3), 775 LP – 783.
506 https://doi.org/10.1681/ASN.2017040380

507 Jernvall, J, Aberg, T., Kettunen, P., Keranen, S., & Thesleff, I. (1998). The life history of an
508 embryonic signaling center: BMP-4 induces p21 and is associated with apoptosis in the mouse
509 tooth enamel knot. *Development*, *125*(2), 161–169.

510 Jernvall, Jukka, Kettunen, P., Karavanova, I., Martin LB, & Thesleff, I. (1994). Evidence for the
511 role of the enamel knot as a control center in mammalian tooth cusp formation: non-dividing cells
512 express growth stimulating Fgf-4 gene. *The International Journal of Developmental Biology*, *38*,
513 463–469.

514 Katz, S. R., Yakovlev, M. A., Vanselow, D. J., Ding, Y., Lin, A. Y., Parkinson, D. Y., Wang, Y.,
515 Canfield, V. A., Ang, K. C., & Cheng, K. C. (2021). Whole-organism 3D quantitative
516 characterization of zebrafish melanin by silver deposition micro-CT. *ELife*, *10*, e68920.
517 https://doi.org/10.7554/eLife.68920

518 Kuan, A. T., Phelps, J. S., Thomas, L. A., Nguyen, T. M., Han, J., Chen, C.-L., Azevedo, A. W.,
519 Tuthill, J. C., Funke, J., Cloetens, P., Pacureanu, A., & Lee, W.-C. A. (2020). Dense neuronal
520 reconstruction through X-ray holographic nano-tomography. *Nature Neuroscience*, *23*(12), 1637–
521 1643. https://doi.org/10.1038/s41593-020-0704-9

522 Metsäranta, M., Toman, D., De Crombrugghe, B., & Vuorio, E. (1991). Specific hybridization
523 probes for mouse type I, II, III and IX collagen mRNAs. *Biochimica et Biophysica Acta (BBA) -*
524 *Gene Structure and Expression*, *1089*(2), 241–243. https://doi.org/https://doi.org/10.1016/0167-
525 4781(91)90014-D

526 Metscher, B. D. (2009a). Micro CT for comparative morphology: Simple staining methods allow
527 high-contrast 3D imaging of diverse non-mineralized animal tissues. *BMC Physiology*, *9*(1),11.
528 https://doi.org/10.1186/1472-6793-9-11

529 Metscher, B. D. (2009b). MicroCT for developmental biology: A versatile tool for high-contrast 3D
530 imaging at histological resolutions. *Developmental Dynamics, 238*(3), 632–640.
531 https://doi.org/10.1002/dvdy.21857

532 Metscher, B. D., & Müller, G. B. (2011). MicroCT for molecular imaging: Quantitative visualization
533 of complete three-dimensional distributions of gene products in embryonic limbs. *Developmental*
534 *Dynamics, 240*(10), 2301–2308. https://doi.org/10.1002/dvdy.22733

535 Mizutani, R., & Suzuki, Y. (2012). X-ray microtomography in biology. *Micron, 43*(2), 104–115.
536 https://doi.org/https://doi.org/10.1016/j.micron.2011.10.002

537 Müller, M., Kimm, M. A., Ferstl, S., Allner, S., Achterhold, K., Herzen, J., Pfeiffer, F., & Busse, M.
538 (2018). Nucleus-specific X-ray stain for 3D virtual histology. *Scientific Reports, 8*(1), 17855.
539 https://doi.org/10.1038/s41598-018-36067-y

540 Ng, L.-J., Wheatley, S., Muscat, G. E. O., Conway-Campbell, J., Bowles, J., Wright, E., Bell, D. M.,
541 Tam, P. P. L., Cheah, K. S. E., & Koopman, P. (1997). SOX9 Binds DNA, Activates Transcription,

and Coexpresses with Type II Collagen during Chondrogenesis in the Mouse. *Developmental Biology, 183*(1), 108–121. https://doi.org/https://doi.org/10.1006/dbio.1996.8487

Pauwels, E., Van Loo, D., Cornillie, P., Brabant, L., & Van Hoorebeke, L. (2013). An exploratory study of contrast agents for soft tissue visualization by means of high resolution X-ray computed tomography imaging. *Journal of Microscopy, 250*(1), 21–31. https://doi.org/10.1111/jmi.12013

Powell, R. D., Hainfeld, J. F., Eisen, R. N., & Tubbs, R. R. (2002). Enzymatic Metallography: a Simple New Staining Method. *Microscopy and Microanalysis, 8*(S02), 916–917. https://doi.org/10.1017/S1431927602107264

Powell, R. D., Pettay, J. D., Powell, W. C., Roche, P. C., Grogan, T. M., Hainfeld, J. F., & Tubbs, R. R. (2007). Metallographic in situ hybridization. *Human Pathology, 38*(8), 1145–1159. https://doi.org/https://doi.org/10.1016/j.humpath.2007.05.004

Raj, M. T., Prusinkiewicz, M., Cooper, D. M. L., George, B., Webb, M. A., & Boughner, J. C. (2014). Technique: Imaging earliest tooth development in 3D using a silver-based tissue contrast agent. *Anatomical Record, 297*(2), 222–233. https://doi.org/10.1002/ar.22845

Rawson, S. D., Maksimcuka, J., Withers, P. J., & Cartmell, S. H. (2020). X-ray computed tomography in life sciences. *BMC Biology, 18*(1), 21. https://doi.org/10.1186/s12915-020- 549 0753-2

Rosen, B., & Beddington, R. S. P. (1993). Whole-mount in situ hybridization in the mouse embryo: gene expression in three dimensions. *Trends in Genetics, 9*(5), 162–167. https://doi.org/https://doi.org/10.1016/0168-9525(93)90162-B

Sakai, K., Hiripi, L., Glumoff, V., Brandau, O., Eerola, R., Vuorio, E., Bösze, Z., Fässler, R., & Aszódi, A. (2001). Stage-and tissue-specific expression of a Col2a1-Cre fusion gene in transgenic mice. *Matrix Biology, 19*(8), 761–767. https://doi.org/https://doi.org/10.1016/S0945- 559 053X(00)00122-0

566 Sandberg, M., & Vuorio, E. (1987). Localization of types I, II, and III collagen mRNAs in developing
567 human skeletal tissues by in situ hybridization. *The Journal of Cell Biology, 104*(4), 1077–1084.
568 https://doi.org/10.1083/jcb.104.4.1077

569 Schindelin, J., Arganda-Carreras, I., Frise, E., Kaynig, V., Longair, M., Pietzsch, T., Preibisch, S.,
570 Rueden, C., Saalfeld, S., Schmid, B., Tinevez, J.-Y., White, D. J., Hartenstein, V., Eliceiri, K.,
571 Tomancak, P., & Cardona, A. (2012). Fiji: an open-source platform for biological-image analysis.
572 *Nature Methods, 9*(7), 676–682. https://doi.org/10.1038/nmeth.2019

573 Schulte-Merker, S., Ho, R. K., Herrmann, B. G., & Nusslein-Volhard, C. (1992). The protein product
574 of the zebrafish homologue of the mouse T gene is expressed in nuclei of the germ ring and the
575 notochord of the early embryo. *Development, 116*(4), 1021–1032.
576 https://doi.org/10.1242/dev.116.4.1021

577 Thisse, C., & Thisse, B. (2008). High-resolution in situ hybridization to whole-mount zebrafish
578 embryos. *Nature Protocols, 3*(1), 59–69. https://doi.org/10.1038/nprot.2007.514

579 Weipoltshammer, K., & Schöfer, C. (2000). Signal enhancement at the electron microscopic level
580 using Nanogold and gold-based autometallography. *Histochem Cell Biol, 114*(6), 489–495.
581 https://doi.org/10.1007/s004180000217

582 Yu, J. K. S., & Holland, L. Z. (2009). Amphioxus Whole-Mount In Situ Hybridization. *Cold Spring*
583 *Harbor Protocols, 2009*(9),
584 pdb.prot5286.http://cshprotocols.cshlp.org/content/2009/9/pdb.prot5286.abstract

585 Zysk, A. M., Garson, A. B. 3rd, Xu, Q., Brey, E. M., Zhou, W., Brankov, J. G., Wernick, M. N.,
586 Kuszak, J. R., & Anastasio, M. A. (2012). Nondestructive volumetric imaging of tissue
587 microstructure with benchtop x-ray phase-contrast tomography and critical point drying. *Biomedical*
588 *Optics Express, 3*(8), 1924–1932. https://doi.org/10.1364/BOE.3.001924